# Modeling of GP(I) zone formation during quench in an industrial AA7449 75 mm thick plate

P. Schloth [a,b], A. Deschamps [c,d], Ch.-A. Gandin [e,f], J.-M. Drezet [a,*]

[a] Ecole Polytechnique Federale de Lausanne, Computational Materials Laboratory, station 12, 1015 Lausanne, Switzerland
[b] Paul Scherrer Institut, Materials Science and Simulation, ASQ/NUM, 5232 Villigen PSI, Switzerland
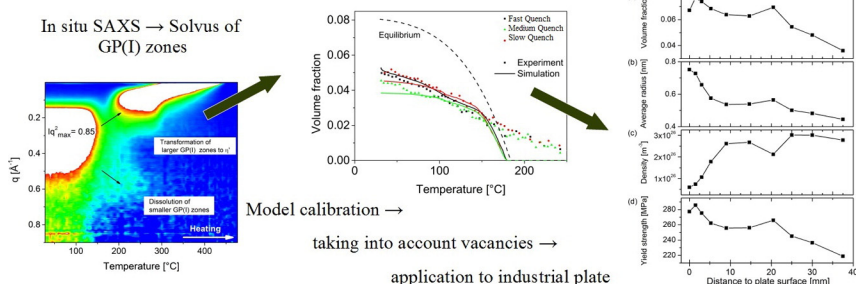[c] Univ. Grenoble Alpes, SIMAP, 38000 Grenoble, France
[d] CNRS, SIMAP, 38000 Grenoble, France
[e] CNRS, CEMEF UMR 7635, 06904 Sophia Antipolis, France
[f] MINES ParisTech, 06904 Sophia Antipolis, France

GRAPHICAL ABSTRACT



Modeling of GP(I) zone formation during quench in an industrial AA7449 75 mm thick plate

ARTICLE INFO

ABSTRACT

The GP(I) zone formation during quench is simulated in an industrial Aluminum alloy AA7449 75 mm thick plate by using a multi-class precipitation model. For this purpose, results of in situ SAXS experiments are reported. A methodology is presented that takes advantage of the collected data to derive *i* - a thermodynamic description for GP(I) zones from reversion heat treatments by using a solubility product and *ii* - the influence of excess vacancies on diffusion coefficients. This approach allows reproducing reasonably well the GP(I) zone formation measured during rapid cooling. Further, the simulated as-quenched surface yield strength compares well with experimental results reported in the literature.

© 2016 Published by Elsevier Ltd.

## 1. Introduction

Heat treatable Al-Zn-Mg(-Cu) Aluminum alloys (AA7xxx) are widely used as structural components owing to their high specific strength, low corrosion susceptibility and high damage tolerance. The fabrication of AA7xxx Aluminum alloys requires a number of thermo-mechanical steps, ending with the age-hardening treatment, which is tailored to adjust the mechanical properties to the end product.

The age-hardening treatment consists of solutionizing, quenching, stretching and multi-step aging along the typical precipitation sequence leading to the equilibrium η phase ($Mg(Zn,Cu,Al)_2$) in the Al-Zn-Mg(-Cu)

* Corresponding author.
  E-mail address: jean-marie.drezet@epfl.ch (J.-M. Drezet).

system: GP(I) zones → η′ → η [1]. This precipitation sequence has received a number of refinements, which have shown that depending on the alloy composition and thermal treatment (isothermal vs. non-isothermal, temperature range) several types of GP zones of different morphology could be formed, leading to different sub-types of η′ precipitates [2–4]. The quenching step from the solution treatment temperature is particularly critical, as it must be adjusted to balance between two contradictory effects, namely quench-induced coarse precipitation with sizes around 100 nm, and the generation of internal stresses that result from thermal gradients which induce thermal strains and inhomogeneous plastic strain near the surface of the quenched parts. Residual stresses increase in magnitude with the size of the parts because of higher thermal gradients between the surface and the center [5]. Different processes can be applied to reduce the residual stresses, such as stretching that is commonly used for plates. For complex geometries as in the case of forgings stress relief is not always possible. Yet, residual stresses cannot be removed completely and part distortions can still occur [6,7], which make final shape corrections necessary, thereby increasing the manufacturing time cycle and costs [8].

In addition to the formation of residual stresses it has been evidenced that lower cooling rates in larger products can lead to material property variations due to quench-induced precipitation [9]. The heterogeneous formation of the coarse equilibrium η phase has been evidenced at high temperatures during quench, predominantly on grain boundaries and dispersoids [1,10]. The formation of these coarse η precipitates has a detrimental effect on the final mechanical properties [1, 11,12] and decreases the yield strength during quench [13]. A limited number of studies have simulated this heterogeneous precipitation during quench [9,14].

In contrast, homogeneous precipitation during quench has received little attention since the temperature changes during quench are usually rapid and this homogeneous precipitation is difficult to deconvolute from the subsequent natural aging that occurs rapidly after the end of the quench. Zhang et al. evidenced low temperature precipitation during fast cooling by using DSC from 250 to 150 °C in a commercial AA7150 alloy, which they first ascribed to the homogeneous nucleation of the η′ phase [15]. In a more recent study, it was shown that this low temperature reaction originated from the precipitation of the platelet shaped Y-phase. The Y-phase features a high aspect ratio and a similar structure as the $T_1$ (Al$_2$CuLi) phase, which is observed in Al-Cu-Li alloys [16]. Schloth et al. evidenced by in-situ SAXS measurements the formation of nanosized precipitates in the AA7449 alloy during cooling close to industrial practice, which harden the material during quench [17]. The size of these precipitates was observed to be consistent with the formation of GP zones.

An attempt to simulate quench-induced homogeneous precipitation was first proposed by Godard but he could not verify his results against experimental findings [9]. Recently, Starink et al. proposed a model for linear cooling and strengthening in Al-Zn-Mg-Cu alloys taking into account the formation of three phases during cooling. Their modeling approach considers the formation of the S (Al2CuMg) phase at high temperature, the η phase at medium temperature and a Zn—Cu rich platelet phase at lower temperature between 250 °C and 150 °C [18].

Precipitation simulations during cooling can be linked with a thermo-mechanical model in order to investigate the influence of precipitation on residual stress predictions as shown by Godard [9]. In the case of a 400 mm AA7010 thick plate the influence was small. However, Chobaut et al. recently stated that the residual stress formation during quench in thick AA7449 plates requires considering the influence of this homogeneous low-temperature precipitation on the mechanical properties [19]. As will be shown in Section 3.1, these low-temperature precipitates formed during rapid cooling give rise to isotropic small-angle scattering and therefore must be of near-spherical shape. Therefore, in the following we will consider that they consist mainly of GP(I) zones and that other phases of high aspect ratio, such as the GPII zones or the Y phase, can be neglected.

The formation kinetics of GP(I) zones at room temperature has been the subject of several studies [20,21,22]. The GP(I) zone formation was attributed to the migration of Mg-vacancy complexes, which was supported by apparent activation energy of 0.69 eV [20]. Kenesei et al. evidenced that the GP(I) zones nucleate at room temperature after quenching and grow in size and volume fraction with time. This study was based on in-situ small-angle X-ray scattering [21]. Further, they showed that the growth of GP(I) zones was controlled by the migration of Zn and that Cu slowed down the precipitation kinetics at room temperature.

The aim of the present paper is to develop a simulation of the formation of GP(I) zones during quenching which is capable of accounting for the major precipitation effect on the residual stress formation. The methodology is based on an experimental study which consists in quantifying the kinetics of GP(I) zone formation during quenching and subsequent reversion heat treatments. This experimental study allows developing a model for the formation of GP(I) zones using a dedicated thermodynamic description and taking into account the influence of excess vacancies on diffusion.

## 2. Experimental and numerical methods

### 2.1. Materials

In this work, the commercial AA7449 Aluminum alloy was used. It was provided as as-quenched (and natural aged) plate with a thickness of 75 mm by Constellium C-TEC (Voreppe, France). The range of chemical composition of the alloy is Al - [7.5, 8.7] Zn - [1.8, 2.7] Mg - [1.5, 2.3] Cu (in wt.%). The specimen size was 3 mm × 25 mm × 0.5 mm. They were taken from the quarter thickness of a 75 mm plate to ensure a similar composition for the investigated samples since macrosegregation is common in thick plates. The samples were then solutionized for 1 h at 474 °C and quenched in water to dissolve all residual precipitation. The remaining minor quantities of intermetallic such as Al7Cu2Fe and dispersoids such as Al3Zr did not change during the experimental study.

### 2.2. Small-angle scattering

Fast time-resolved SAXS experiments were performed at the cSAXS beamline of the Swiss Light Source (SLS) at the Paul Scherrer Institut (PSI) (Villigen, Switzerland), at a wavelength of 0.774 Å (16 keV) with a beam size of 200 μm × 200 μm. The range of accessible momentum transfers was 0.007 Å$^{-1}$ ≤ q ≤ 1 Å$^{-1}$. A laser-based heating system was used to apply the different heat treatments. The experimental setup is explained in more detail in reference [17]. SAXS images were recorded every 0.5 s to follow the dynamic processes during the various heat treatments. The samples 3 mm × 25 mm × 0.5 mm in size were solution treated with subsequent quench into water and stored in a freezer prior to the SAXS experiments. Before each in situ quench, the samples were solution treated for 7 min at 474 °C to homogenize the microstructure. The quench intensity was designed to reproduce the cooling of the alloy at different distances from the plate surface. Different cooling rates were achieved by controlling the thermal gradient between the sample holder and the heating spot on the sample. The fastest cooling (20–100 K s$^{-1}$ at high temperature) was achieved by shutting of the laser; medium and slow cooling rates (20–0.5 K s$^{-1}$) were reached using a PID control. At lower temperature, Newtonian cooling took place. These three quenches are compared with cooling curves measured in the 75 mm thick plate during water quenching at Constellium laboratory in Fig. 1. The medium quench (MQ) is close to what happens at the plate center (mid thickness) whereas the fast quench (FQ) reproduces the cooling of the plate not at the surface but at some distance beneath the surface. The slow quench (MQ) reproduces the cooling at center of thicker plates, e.g. 140 mm in thickness.

The SAXS experiments of long duration were performed on a laboratory rotating anode at the SIMAP laboratory in Grenoble. A Cu K$_\alpha$ source
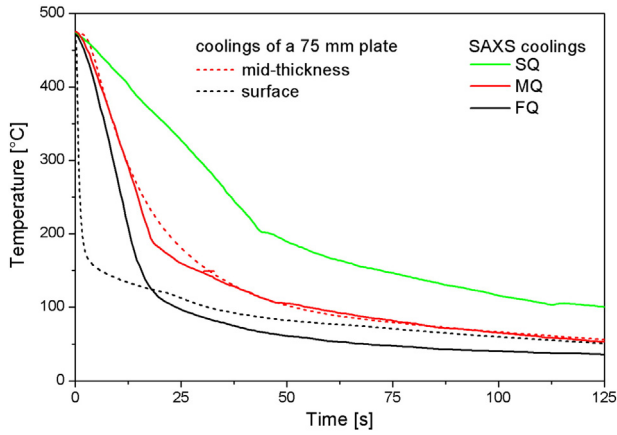
Fig. 1. Measured cooling curves in a 75 mm thick plate at center plane (mid thickness) and surface during water quenching and comparison with the SAXS quenches. FQ refers to fast quench, MQ to medium quench and SQ to slow quench, respectively.

was used giving a wavelength of 1.54 Å (8 keV). The samples featured typically a thickness of 80–120 μm. The size of the X-ray beam was 1 mm × 1 mm giving an illuminated volume of roughly 1 mm × 1 mm × 0.1 mm. Reversion heat treatments were carried out using a dedicated furnace [23]. The signal was recorded with a CCD camera. The accessible range of scattering vectors was limited to 0.04 Å$^{-1}$ ≤ q ≤ 0.5 Å$^{-1}$. The samples were in the T4 state, i.e. containing only GP(I) zones, before they were heated to 300 °C ± 2 °C with heating rates 1 and 5 K min$^{-1}$. The measurement times for one image were 150 s and 30 s for 1 K min$^{-1}$ and 5 K min$^{-1}$, respectively.

The intensity was azimuthally averaged for each scattering vector since the 2D SAXS images revealed isotropic scattering for all scattering angles. The scattering spectra were corrected for electronic noise, flat field of detector, and background. The absolute intensity was normalized using glassy carbon as a secondary standard [24].

The structural parameters such as precipitate radius and volume fraction were estimated by assuming spherical precipitates and using a model independent analysis as described by Deschamps and de Geuser [25]. More details about the applied procedure can be also found in Reference [17]. In addition, it has to be mentioned that the relative uncertainties of the volume fraction calculations cannot be expected to be better than ± 10%. This is due to the uncertainties related to the absolute intensity calibration, the extrapolations of the data to 0 and infinity, and the assumptions of the chemical composition of the precipitates [26].

The SAXS spectra at the end of the cooling were additionally subjected to model dependent analysis by using the SASfit software [27]. The form factor of a sphere was used and the lognormal size distribution was assumed to simulate the scattering signal of GP(I) zones and in order to derive the precipitate size distribution at the end of rapid cooling.

### 2.3. Precipitation and yield strength model

A classical thermodynamic based nucleation and growth model of Eulerian type was used in this study. A detailed description of the model is found in Reference [28]. A solubility product approach was developed to establish a thermodynamic description for the GP(I) zones. The regular solution model is only valid when the alloy is sufficiently dilute, which is a reasonable assumption for most commercial AA7xxx alloys. The chemical composition of the GP(I) zones was assumed to be AlZnMg, in agreement with literature [29,30]. Yet, this is a crude assumption as the chemical composition can change as a function of

temperature and aging time [29,31]. The relationship between the solubility limits of Zn and Mg in the Al matrix can then be written as [32]:

$$\left(X_{eq}^{Zn}\right)\left(X_{eq}^{Mg}\right) = \exp((-\Delta H_0/RT) + (\Delta S_0/R)) \quad (1)$$

where $X_{eq}^{Zn}$ and $X_{eq}^{Mg}$ are equilibrium solubility limits in the solid solution [mol. fraction] and $\Delta H_0$ and $\Delta S_0$ are the enthalpy [J mol$^{-1}$] and entropy [J K$^{-1}$ mol$^{-1}$] of formation of the phase, respectively. The solvus boundary of the GP(I) zones was estimated from the change in volume fraction during several dissolution heat treatments. The volume fraction was normalized to its initial value because this normalization allows compensating the uncertainties on the volume fraction measurements and providing a consistent measurement of the dissolution kinetics. The absolute volume fraction $f_v$ of the thermodynamic description is calculated by using a simplified solute balance:

$$f_v = \left(X_0^{Mg} - X_{eq}^{Mg}\right)/X_P^{Mg} \quad (2)$$

where $X_0^{Mg}$ is the gross Mg content of the alloy and $X_P^{Mg}$ is the Mg content in the precipitate. Such thermodynamic description is relevant enough for studying the effect of quench rate.

The influence of vacancies on the diffusion rate was considered by using adapted diffusion coefficients for Zn and Mg. To this aim, the supersaturation of vacancies, S, was calculated as

$$S = X_v/X_{v,eq} \quad (3)$$

where $X_v$ is the vacancy site fraction [mol. fraction] and $X_{v,eq}$ is the equilibrium vacancy site fraction [mol. fraction]. The equilibrium vacancy site fraction was calculated using the modified Lomer equation proposed in reference [33]

$$X_{v,eq} = A \exp(-H_0/(RT))\{1 - 13(X_{Zn} + X_{Mg})\} + 12X_{Zn} \exp(E_{Zn-v}/(RT)) + 12X_{Mg} \exp(E_{Mg-v}/(RT)) \quad (4)$$

In this equation, A is a constant, T is the temperature [K], $H_0$ is the enthalpy of vacancy formation [J mol$^{-1}$], $X_{Zn}$ and $X_{Mg}$ are the concentration of Zn and Mg atoms [mol. fraction], and $E_{Zn-v}$ and $E_{Mg-v}$ are the binding energies between Zn and Mg atoms and vacancies [J mol$^{-1}$], respectively. The condensation rate of the concentration of excess vacancies is controlled by the vacancy diffusion, $D_v$ [m$^2$ s$^{-1}$], which is expressed for mono vacancies as:

$$D_v = C_E a^2 \exp(-H_m/RT) \quad (5)$$

where $C_E$ is the Einstein constant [s$^{-1}$], a is the lattice parameter [m] and $H_m$ is the migration energy of the vacancies [J mol$^{-1}$]. The annihilation rate $\partial X_v/\partial t$ [s$^{-1}$] depends on the vacancy supersaturation and also on the density of sinks. A simplified equation based on Fick's law was proposed by Godard [9], which takes only one type of vacancy sinks into account:

$$\partial X_v/\partial t = -(X_v - X_{v,eq})/\tau \quad (6)$$

where $\tau$ is the characteristic time [s], which can be calculated as:

$$\tau = (l/2\pi)^2/D_v \quad (7)$$

where l is the distance between the vacancy sinks [m]. The initial value of the vacancy concentration, $X_v$, is the equilibrium vacancy concentration at the solutionizing temperature, $X_{v,eq}$. Subsequently, the annihilation rate $\partial X_v/\partial t$ was calculated for each time step during the heat treatments that followed the solutionizing treatment.

The enthalpy of vacancy formation $H_0$, vacancy migration energy $H_m$ and characteristic diffusion length l were adjusted with experimental data presented in reference [17]. The values of $H_0 = 68,000$ J mol$^{-1}$,

$H_m = 68,007$ J mol$^{-1}$ and $l = 0.25 \cdot 10^{-6}$ m allowed us to simulate the measured evolution of the precipitate radius and volume fraction during a fast quench (FQ), a medium quench (MQ) and slow quench (SQ). The binding energies between vacancies and Zn and Mg atoms were assumed to be 12,520 and 24,080 J mol$^{-1}$ as in [9] although first-principles analysis by Wolverton [34] yielded much lower values.

The supersaturation of vacancies increases the diffusion so that the effective diffusion of an element, $D_{eff}$, is calculated as:

$$D_{eff} = SD_0 \exp(-Q/RT) \tag{8}$$

where $D_0$ is the diffusion constant [m$^2$ s$^{-1}$] and $Q$ is the activation energy of the element in the matrix [J K$^{-1}$ mol$^{-1}$]. The adapted diffusion coefficients were fitted using the Arrhenius law to determine the effective diffusion parameter $D_{0,eff}$ and $Q_{eff}$ used as input for the precipitation modeling in the lower temperature regime between 40 °C and 220 °C.

### 2.3.1. Yield strength model

The yield strength at room temperature, $\sigma_{YS}$ [MPa], was calculated by using an additive strength law as proposed by Fribourg et al. [35]:

$$\sigma_{YS} = \Delta\sigma_0 + \Delta\sigma_{SS} + \Delta\sigma_P = 10 \text{ MPa} + K_{SS}X^{2/3} + pM\mu\sqrt{f_v R_{av}/b} \tag{9}$$

where $\Delta\sigma_0$ is a constant, 10 MPa for the present aluminum alloy, originating from the lattice friction, the dislocations and the grain boundaries, $\Delta\sigma_{SS}$ is the solid solution strength [MPa] and $\Delta\sigma_P$ is the strength contribution due to shearable precipitates [MPa]. X is the global solute content in the solid solution defined as $X_{Zn} + X_{Mg} + X_{Cu}$ and $K_{SS}$ is the average strengthening coefficient [MPa (mol. fraction)$^{-2/3}$]. M is the Taylor factor, $\mu$ is the shear modulus [MPa], $f_v$ is the volume fraction of the precipitates, $R_{av}$ is the average radius of the precipitates and b is the Burgers vector [m]. The parameters, $K_{SS} = 800$ MPa (mol. fraction)$^{-2/3}$ for the solid solution contribution and p = 0.00665 for the precipitate shearing contribution, were calibrated against results obtained by in situ SAXS experiments and Gleeble measurements [36, 37,38]. The global parameter $K_{SS}$ was calibrated from the as-quenched yield strength of the AA7449 alloy. Tensile tests were performed directly after rapid cooling in the range $-50$ to $-80$ K s$^{-1}$ from the solutionizing temperature to room temperature in a Gleeble machine. The parameter p of the precipitate shearing law was calibrated by performing the same cooling conditions with the Gleeble machine as done for the in situ SAXS experiments. The microstructural information, such as precipitate size and volume fraction, estimated from SAXS measurements were linked with the mechanical properties obtained by the Gleeble tests.

## 3. Results and discussion

### 3.1. Thermodynamic description of GP(I) zones

#### 3.1.1. Nature of the quench-induced nano-sized precipitates

It has been recently shown that nano-sized clusters, i.e. regions of higher solute concentration, form in the AA7449 alloy during quenching close to industrial practice [17]. SAXS measurements revealed the formation or dissolution of these nano-sized clusters but their nature remained unclear. In order to characterize their nature, the dissolution behavior of these quench-induced clusters was compared to the dissolution behavior of GP(I) zones during heating.

Fig. 2 shows a typical 2D-SAXS image, which is representative for the precipitation state at the end of a rapid cooling. This image presents the un-normalized data, i.e. the number of ADUs (CCD counting units) per pixel. Low q values are reached close to the center (direct beam) of the 2D image behind the beam stop. High q values are met further away from the center/direct beam. Scattering effects are visible in the low q-region close to the beam stop. This scattering effect at low q indicates large scattering objects, which are most likely due to the formation
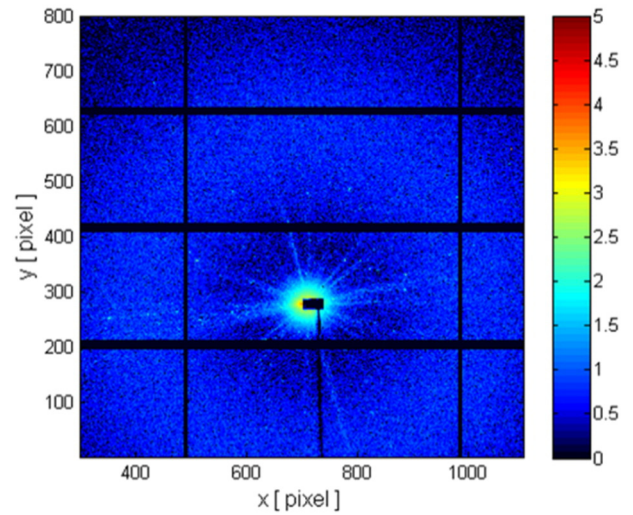


**Fig. 2.** 2D SAXS image representing the precipitation state at the end of a rapid cooling.

of the η precipitates at high temperatures during rapid cooling. Scattering is also visible in the high q-region, with a ring of scattering intensity. This scattering effect is isotropic, which indicates that the main precipitation phase in the high q-region has a spheroidal shape. The fact that a scattering ring is observed (i.e. a maximum of scattering intensity vs. q is present) means that the distance between clusters is of the same order as their size. Clusters with a blocky structure [29], GP(I) zones and the Y-phase [16] have been evidenced in Al-Zn-Mg-Cu alloys after fast cooling. Yet, phases with a high aspect-ratio such as GP(II) zones [17], the Y-phase or $T_1$ (Al$_2$CuLi) phase lead to a highly non-isotropic scattering pattern [39]. The Y-phase was evidenced after linear cooling with $-10$ to $-30$ K s$^{-1}$ in a AA7150 alloy, which feature a much lower Zn content and a slightly elevated Cu content compared to the AA7449 alloy. Therefore, in the following we will consider that precipitates with a spherical shape dominate in the AA7449 alloy for cooling conditions close to industrial practice and that the Y-phase plays only a minor role if present.

Fig. 3 illustrates the heat treatment performed on a AA7449 sample that was initially in the T4 state. The sample was heated up with an average rate of 7 K s$^{-1}$ to the solutionizing temperature and held for 7 min before it was cooled down at a rate between 20 and 30 K s$^{-1}$ to form quench-induced clusters, corresponding to industrial practice [38]. After quenching the sample was heated up again with an average rate of 5 K s$^{-1}$ to the solutionizing temperature.

The corresponding SAXS data for the dissolution of the GP(I) zones initially present in the T4 state and for the dissolution of the quench-induced precipitates are shown in Fig. 3b and c, respectively. The scattering curves are shown in Kratky representation (I.q$^2$ vs. q where I is the scattered intensity and q the scattering vector) as a function of temperature. The intensity is illustrated by the colour of the 2D image, where low scattering is in blue and high scattering in red or white when the intensity is higher than 0.25 Å$^{-5}$. The maximum of 0.25 Å$^{-5}$ was chosen to better observe the scattering peak resulting from the quench-induced clusters in Fig. 3c.

A broad scattering peak due to GP(I) zones is visible at a q-value of 0.3 Å$^{-1}$ before heating in Fig. 3b. The absence of scattering at low q values shows that no heterogeneous η precipitates were formed during the quench preceding the T4 initial temper of the sample. Upon heating the GP(I) zones scattering peak is stable until 100 °C. With further heating the intensity of the GP(I) zones peak at high-q values starts to decrease. This is due to the dissolution of smaller particles, which become unstable (Gibbs Thomson capillarity effect). Fig. 3b shows that around 150 °C the GP(I) zones scattering peak has decreased drastically. With further increasing temperature around 170 °C the scattering peak splits into two parts, which indicates two different phenomena. The
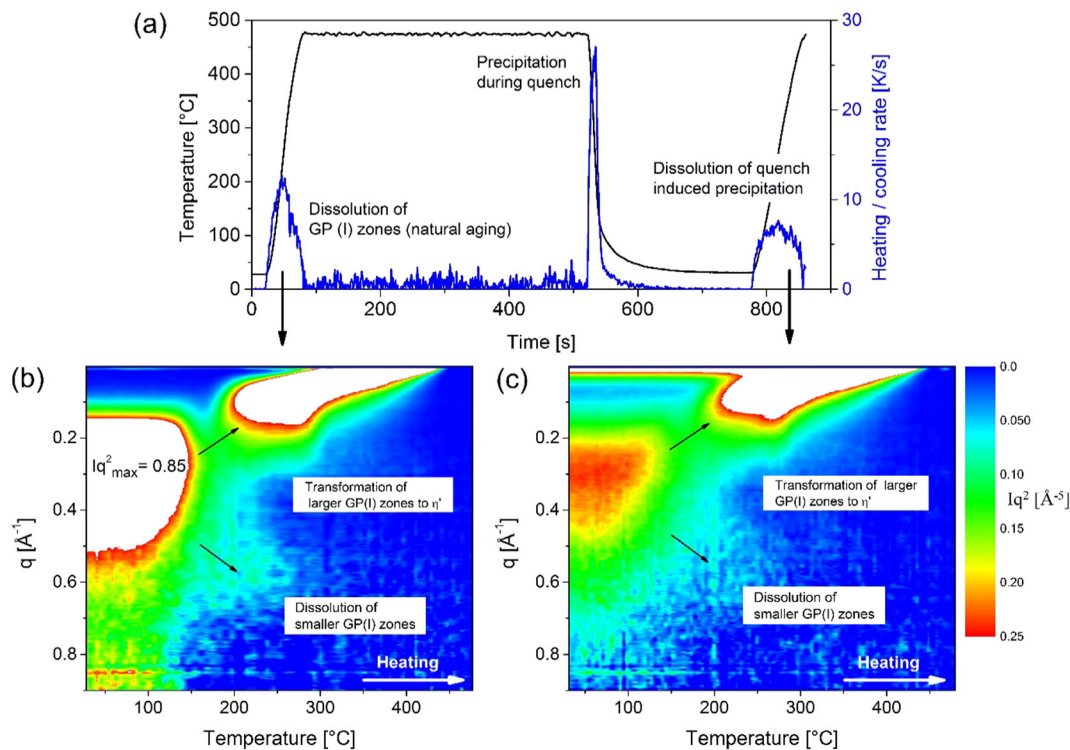
**Fig. 3.** Precipitation sequence for a AA7449 sample deduced from in situ SAXS analyses showing (a) the temperature history and the corresponding heating/cooling rates and the evolution of the scattering signal upon heating after (b) natural aging and (c) quenching at a rate between 20 and 30 K s$^{-1}$. Heating is performed at around 7 K s$^{-1}$, long enough after quenching so that the sample has cooled down at room temperature. The Kratky plots are shown as function of temperature, where the intensity scales in the colored scale bar. The intensity was scaled to a value of 0.25, which presents the intensity maximum of the high-q peak in (c).

smaller GP(I) zones dissolve completely between 200 and 250 °C. The larger GP(I) zones seem to remain stable and transform into $\eta'$ precipitates as indicated by the connected scattering peaks. Alternatively, they also have dissolved and $\eta'$ forms from the solid solution. Yet, this point cannot be clarified only from the scattering data. The $\eta'$ precipitates grow with further heating and transform into $\eta$, which is evidenced by a shift of the scattering peak to lower q values. Around 300 °C, $\eta$ starts to dissolve but continues to grow until 440 °C when the scattering signal shifts to lower q and finally disappears from the measured q-range. These dissolution temperatures are in the range of those measured by Puydt et al. on an AA7020 alloy [40].

Fig. 3c shows the dissolution of the quench-induced clusters which looks very similar to the dissolution of the GP(I) zones presented in Fig. 3b. At the end of the cooling from the solutionizing temperature, a scattering peak due to the quench-induced clusters is seen, yet with a smaller intensity compared to the GP(I) zones of the T4 material, revealing a smaller volume fraction of scattering objects. In addition, at lower q values scattering is observed that originates from the quench induced heterogeneous $\eta$ precipitates. Increasing the temperature leads to the dissolution of the quench-induced precipitates in a similar manner compared to the GP(I) zones of the T4 material. A small difference is that the shift of scattered intensity to lower q-values starts slightly earlier compared to the T4 material. This small difference can be related to either the smaller heating rate (5 K s$^{-1}$ vs 7 K s$^{-1}$) and/or a higher amount of excess vacancies directly after quench compared to natural aging of 4 days, which enhances the solute transport.

The trends observed in the scattering plots are supported by the quantitative analysis. Fig. 4 shows quantitatively the evolution of the GP(I) zones and quench-induced clusters in terms of Guinier radius and volume fraction upon heating. In the naturally aged material, the volume fraction and radius of the GP(I) zones (10% and 0.6 nm) is higher compared to that of the quench-induced clusters (5% and 0.5 nm). Between 80 and 150 °C the volume fraction decreases and the average radius increases in both cases. The average radius increases

due to the dissolution of smaller particles. The splitting of the precipitate size distribution takes place earlier for the quench-induced clusters (100 °C) compared to the GP(I) zones (150 °C), which can be linked to the smaller size and volume fraction. The increasing radius between 150 and 200 °C could be related to the appearance of $\eta'$, which also stabilizes the volume fraction. $\eta'$ is seen to form earlier in the case of the quench-induced clusters. As mentioned before, this can be due to the slower heating rate and/or a higher concentration of non-equilibrium vacancies. Further heating shows an increasing radius of $\eta'$ and $\eta$ and decreasing volume fraction from around 300 °C until 470 °C.

The dissolution behavior of the quench-induced precipitates is very similar to the dissolution of the GP(I) zones that formed during natural
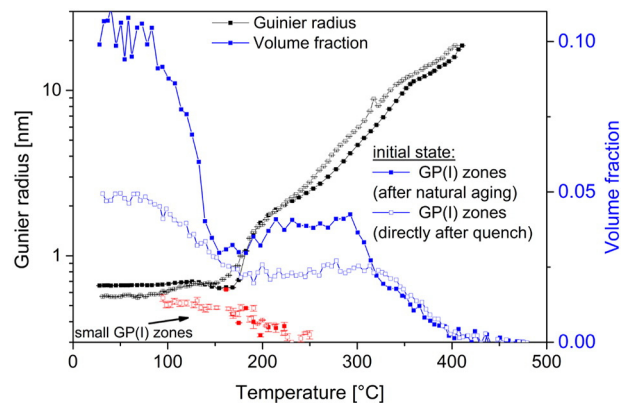


**Fig. 4.** Evolution of the Guinier radius (black) and volume fraction (blue) upon heating is shown for the T4 state (full symbols) and the as-quenched FQ state (open symbols). The size of the smaller precipitates is also shown as red symbols without line. (For interpretation of the references to colour in this figure legend, the reader is referred to the web version of this article.)

aging for 4 days. Therefore, it can be assumed that the precipitates formed during the investigated quench are actually GP(I) zones.

### 3.1.2. Thermodynamic description of GP(I) zones using the solubility product

In order to model the formation of GP(I) zones during quenching a thermodynamic description is required. Since the quench-induced precipitates were characterized as GP(I) zones, a thermodynamic description can be established from GP(I) zones dissolution (reversion) experiments by using the solubility product.

Fig. 5 shows the normalized volume fraction evolution of the different reversion heat treatments that have been performed. The volume fraction was normalized to the initial value near room temperature reported in Fig. 4. The dissolution of the GP(I) zones starts for all average heating rates at around 80 °C and show a similar decrease in volume fraction with further heating, except for the case of 1 K min$^{-1}$, which drops slightly faster. The decrease of the volume fraction stabilizes at temperatures between 140 °C and 180 °C, which is related to the formation of η′ precipitates. The end temperature of the partial reversions shifts to higher values as the heating rate increases. In addition, the volume fraction of GP(I) zones that is present in the sample when η′ appears decreases with increasing heating rates.

Based on the reversion heat treatments and the dissolution behavior of the GP(I) zones a thermodynamic description is established using the solubility product given by Eq. (1). Copper is excluded from the description since it is the slowest diffusing element. Indeed, it was shown in literature that the activation energy of GP(I) zone nucleation and growth is close to the Mg activation energy (0.6 eV ≈ 58,000 J mol$^{-1}$) in Aluminum [20,41]. Therefore, the GP(I) zone formation is controlled by the motion of Mg atoms [42] and not Cu. In addition, the Cu content in GP(I) zones is typically small [29] and increases only after long aging time in the precipitates [31].

The thermodynamic description is obtained by adjusting the parameters $\Delta H_0$ and $\Delta S_0$ so that the normalized volume fraction of the thermodynamic description fits the experimental results in the temperature range [20 °C, 190 °C]. The curvature effect is taken into account by using the measured radius at the end of the reversion heat treatment (0.45 nm) and a typical value for the interfacial energy (0.01 J m$^{-2}$) of coherent precipitates such as GP(I) zones. The calculated equilibrium volume fraction of 8% at room temperature assuming the chemical composition of the GP(I) zones to be AlMgZn is in the range of the experimental values [17,32,35].
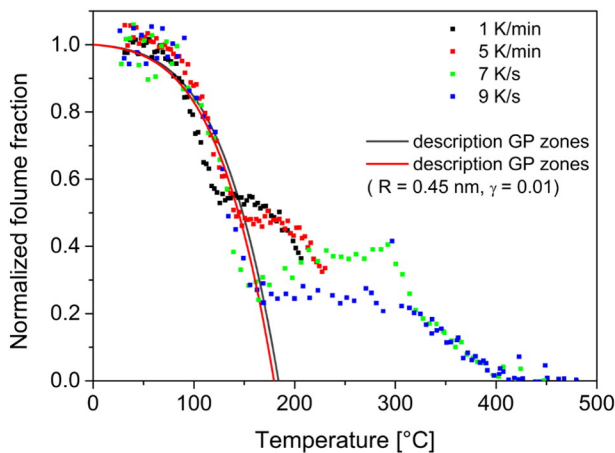


**Fig. 5.** Normalized volume fraction evolution for several reversion heat treatments for the AA7449 alloy in the T4 state. The normalized equilibrium volume fraction is also shown (black line) and the influence of the curvature effect on the solvus boundary is emphasized (red line). The labels indicate an average heating rate for each experiment. (For interpretation of the references to colour in this figure legend, the reader is referred to the web version of this article.)

The thermodynamic description of the GP(I) zones is found to compare well with the dissolution behavior observed for the GP(I) zones in the experiments until the η′ precipitates appear. Good agreement is found for values of 31,000 J mol$^{-1}$ and 11 J mol$^{-1}$ K$^{-1}$ for $\Delta H_0$ and $\Delta S_0$, respectively. These values are in a similar range of what has been reported for Mg—Cu co-clusters in AA2xxx alloys ($\Delta H_0 = 38,000$ J mol$^{-1}$ [43]) and for GP(I) zones in an Al-Zn-Mg alloy ($\Delta H_0 = 48,000$ J mol$^{-1}$, $\Delta S_0 = 10$ J mol$^{-1}$ K$^{-1}$ [33]). The solvus temperature of the GP(I) zones in the AA7449 is then 184 °C, which agrees well with results reported in literature [41].

With the present thermodynamic description, the modeling approach is limited to the solvus boundary of the GP(I) zones. A second description for the η′ phase and a conversion criterion to pass from one phase to the other would be needed to describe for example the complete reversion heat treatments. However, during rapid cooling GP(I) zones were predominantly found to form and control the yield strength evolution during the quench step [17,36], so that the description of this phase only should be sufficient in the present context.

### 3.2. Model calibration

The model was calibrated against the experimental in situ SAXS measurements reported in reference [17]. The model parameters used to simulate the GP(I) zone formation during cooling are presented in Table 1.

The nucleation parameters of the model were adjusted in order to have an average size of GP(I) zones that is close to the experimentally measured size reported in reference [17]. An interfacial energy of 0.01 J m$^{-2}$ and a nucleation site density of $10^{28}$ m$^{-3}$ (if every atom is a nucleation site the density would be 8.6 $10^{28}$ m$^{-3}$) were found to give results in a similar range. The values are representative of the homogeneous nucleation of coherent precipitates.

The parameters used to estimate the excess vacancies, e.g. $H_0$, $H_m$ and $l$, were adjusted in an iterative way so that the modeling results of the three cooling rates (fast quench – FQ, medium quench – MQ and slow quench SQ) match the experimental results. The modeling results depend sensitively on these three parameters and therefore, on the effective diffusion parameter. The 68,000 J mol$^{-1}$ found for $H_0$ is in between the values proposed in literature (67,000 and 72,240 J mol$^{-1}$)

**Table 1**
Model parameters.

| Parameter | Symbol | Value | Unit |
|---|---|---|---|
| Interfacial energy between the GP(I) zone and the FCC aluminum matrix | $\gamma$ | 0.01 | J m$^{-2}$ |
| Nucleation site density of the GP(I) zone | $\rho_{NS}$ | $1 \cdot 10^{28}$ | m$^{-3}$ |
| Molar volume of the GP(I) zone | $V_m$ | $0.7 \cdot 10^{-5}$ | m$^3$ mol$^{-1}$ |
| Formation energy of vacancies | $H_0$ | 68,000 | J mol$^{-1}$ |
| Migration energy of vacancies | $H_m$ | 68,000 | J mol$^{-1}$ |
| Distance between vacancy sinks | $l$ | $0.25 \cdot 10^{-6}$ | m |
| Lattice parameter in the FCC aluminum matrix | $a$ | $4.05 \cdot 10^{-10}$ | m |
| Einstein constant | $C_E$ | $10^{13}$ | s$^{-1}$ |
| Gas constant | $R$ | 8.314 | J mol$^{-1}$ K$^{-1}$ |
| Enthalpy of formation of the GP(I) zone | $\Delta H_0$ | 31,000 | J mol$^{-1}$ |
| Entropy of formation of the GP(I) zone | $\Delta S_0$ | 11 | J mol$^{-1}$ K$^{-1}$ |
| Mg content in the precipitate | $X_P^{Mg}$ | 0.33 | Mole fraction |
| Constant | $A$ | 11 | |
| Binding energy between vacancies and Zn | $E_{Zn-v}$ | 12,520 | J mol$^{-1}$ |
| Binding energy between vacancies and Mg | $E_{Mg-v}$ | 24,080 | J mol$^{-1}$ |
| Number of classes for the particle size distribution | $Nb_{clas}$ | 1000 | |
| Maximum radius for the particle size distribution | $R_{max}$ | $2 \cdot 10^{-8}$ | m |
| Time step | $t_{step}$ | $2 \cdot 10^{-2}$ | s |
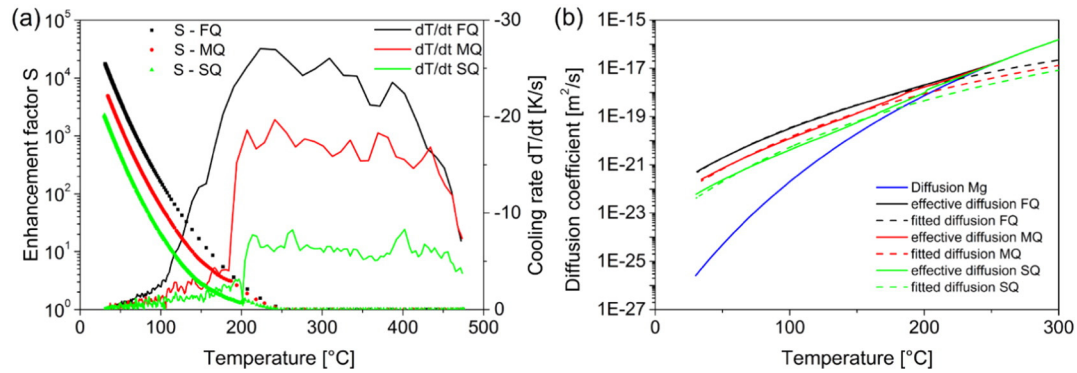
**Fig. 6.** Effect of vacancies on diffusion showing (a) calculated supersaturation of vacancies *S* together with the three cooling rates FQ, MQ and SQ and (b) diffusion coefficients (dashed lines) fitted, (solid lines) calculated for the three cooling's FQ, MQ and SQ, as well as (blue line) reference values. (For interpretation of the references to colour in this figure legend, the reader is referred to the web version of this article.)

[9,44]. The migration energy ($H_m = 68{,}700 \, \text{J} \, \text{mol}^{-1}$) is higher compared to 55,860 and 61,000 J mol$^{-1}$ reported in the references [9,44] but close to the upper limit of the migration energy of vacancies in Al—Cu alloys (41,000–66,900 J mol$^{-1}$) [45]. The characteristic diffusion length for vacancy annihilation, $l = 0.25 \cdot 10^{-6}$ m, is slightly smaller than when annihilation is considered on subgrain size (1–2 $\cdot$ 10$^{-6}$ m), 0.5–1 $\cdot$ 10$^{-6}$ m, or on Al$_3$Zr dispersoids, 0.45 $\cdot$ 10$^{-6}$ m (assuming spherical dispersoids, 15$\cdot$10$^{-9}$ m in radius with a density of 4 $\cdot$ 10$^{19}$ m$^{-3}$ [46]).

### 3.2.1. Effective diffusion coefficients

It was shown in the previous Section that excess vacancies have a marked influence on the activation energy of GP zone formation. Therefore, the influence of excess vacancies on kinetics is taken into account in the modeling of precipitation during cooling by using adapted diffusion coefficients. The excess vacancy concentration was calculated by solving Eqs. (4)–(7) for cooling FQ, MQ and SQ and the supersaturation of vacancies was estimated using Eq. (3).

Fig. 6a shows the calculated supersaturation (enhancement factor *S*) of vacancies together with the cooling rates of FQ, MQ and SQ. In all three cases, the vacancy concentration is in equilibrium until 250 °C but increases with further cooling to room temperature. At the conclusion of the cooling, the highest supersaturation of vacancies is observed for the fastest cooling FQ, which is ten times higher than the supersaturation associated with the slowest cooling SQ.

Using these values for vacancy supersaturation, the effective diffusion coefficient was calculated using Eq. (3) and fitted with modified values for activation energy and pre-exponential factor in the temperature range 40–220 °C. This is exemplarily shown for Mg and the three cooling conditions in Fig. 6b. Similarly to the supersaturation of vacancies, the calculated effective diffusion is highest for FQ, intermediate for MQ and slowest for SQ. The effective diffusion rate of the three cooling schedules deviates at 250 °C from the equilibrium diffusion of Mg and is three to four orders of magnitude higher at room temperature. The fitted effective diffusion coefficients are also presented (dashed lines) for the three cooling's. They represent relatively well the effective diffusion at lower temperatures (20–200 °C). Yet, the quality of the fits decreases from FQ to SQ. In the case of SQ, the diffusion is overestimated between 100 and 150 °C and underestimated below 50 °C. At temperatures higher than 200 °C, the fitted diffusion deviates for the three cases markedly from the effective diffusion. However this has no practical consequence on the modeling result, since the formation of the heterogeneous η phase is not considered here because it is negligible in the 75 mm thick plate as evidenced by SANS measurements in a 75 mm AA7449 thick plate, so that there is no precipitation above 200 °C [36].

The fitted $D_{0,eff}$ and $Q_{eff}$ for the three cooling's are given in Table 2. For FQ, the effective activation energy for Mg (57,700 J mol$^{-1}$) is in a realistic range and almost identical to the migration energy of Mg in

Aluminum (57,900 J mol$^{-1}$) [41]. Cu was not considered in the simulations since it is not present in our thermodynamic description of GP(I) zones. In addition, only Mg diffusion values were used because Zn is diffusing much faster and Mg is therefore the limiting factor. Using the adapted diffusion coefficients for Zn does not change the simulated results.

### 3.2.2. Modeling the GP(I) zone formation during rapid cooling

The volume fraction evolution of GP(I) zones during cooling FQ, MQ and SQ obtained from in situ SAXS results is shown in Fig. 7a together with the modeling results. In addition, the equilibrium volume fraction of GP(I) zones is presented, which is calculated with the established thermodynamic description and the solute balance. In contrast to the experimental results, no GP(I) zone formation can be seen for the modeling above 184 °C since this is their solvus boundary considered in the model. The precipitation observed experimentally at higher temperatures might be due to the formation of more stable phases, likely the η′ phase.

The GP(I) zones form rapidly below their solvus temperature and feature a volume fraction close to the experimental values around 150 °C. The volume fraction evolution modeled for FQ compares very well against the experimental results during further cooling from 150 °C to room temperature. The experimental outcome shows that the volume fraction of GP zones forming during cooling is almost insensitive to the cooling rate. This feature, which is at first sight counterintuitive, is well reproduced by the model. From the model it is possible to state that this experimental finding is due to the compensation of a lower time allowed for precipitation (when the quench rate is faster) by a higher vacancy supersaturation. It is quite a different situation from what happens at higher temperature, where the precipitated volume fraction during quenching has been observed to depend strongly on quench rate [47], because at higher temperature (typically above 200 °C) the vacancy concentration is predicted to remain close to equilibrium.

For the cooling schedules MQ and SQ, the predicted evolution of volume fraction is very similar to the experimental one between 150 and 80 °C. But further cooling leads to deviations and lower volume fraction

**Table 2**
Diffusion parameters of Zn, Cu and Mg and the fitted effective diffusion parameters for Mg for the cooling's FQ, MQ and SQ.

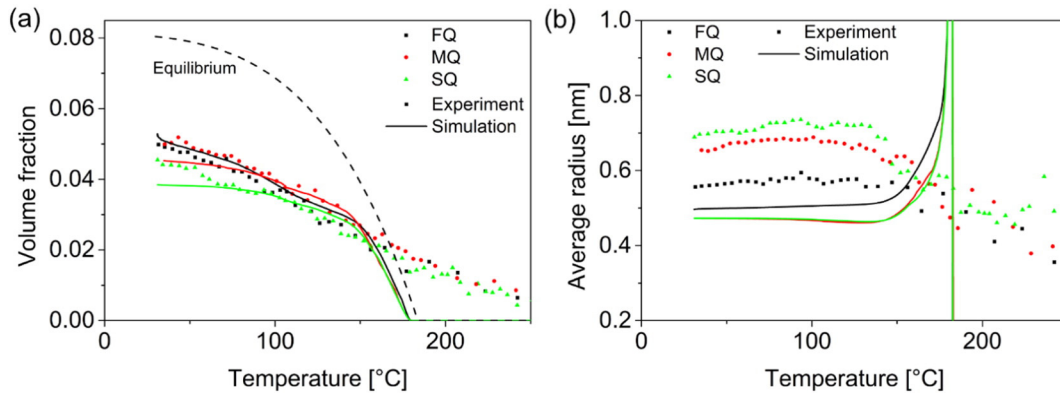| Cooling | $D_{0,eff}$ [m$^2$ s$^{-1}$] | $Q_{eff}$ [J mol$^{-1}$] |
|---|---|---|
| Zn | 1.19 · 10$^{-5}$ ($D_0$) | 116,100 (Q) |
| Cu | 1.49 · 10$^{-5}$ ($D_0$) | 120,500 (Q) |
| Mg | 6.54 · 10$^{-5}$ ($D_0$) | 133,900 (Q) |
| FQ | 4.04 · 10$^{-12}$ | 57,700 |
| MQ | 4.58 · 10$^{-12}$ | 60,800 |
| 0 | 7.68 · 10$^{-12}$ | 64,400 |

**Fig. 7.** Evolution of (a) the volume fraction and (b) the average radius during the three cooling schedules FQ, MQ and SQ obtained from (points) in situ SAXS experiment and (solid lines) precipitation modeling. The equilibrium volume fraction of the GP(I) zones is shown as a dashed black line.

for the modeling results. The observed differences for the simulated and experimental volume fractions may be related to the fitting of the adapted diffusion coefficients as explained in the previous section and shown in Fig. 6b.

The evolution of the simulated average radius is presented in Fig. 7b together with the measured Guinier radius, which is close to the average radius of the precipitates when their size distribution features a dispersion around 0.2. For all three cooling schedules, the simulated initial radius of the GP(I) zones is high due to the small undercooling but decreases rapidly with decreasing temperature due to a decreasing critical radius. At 150 °C the average radius is higher for FQ than for MQ and SQ, both of them showing the same evolution. During further cooling to room temperature the average radius decreases slightly for FQ to 0.5 nm. In contrast, the average radius increases slightly for MQ and SQ and reaches 0.47 nm at the end of the cooling.

In general, the modeled average radius is lower compared to the experimental results. On the one hand, the experiments showed that slower cooling results in a larger radius. This is not supported by the simulations, which give the highest radius for the highest cooling rate. Further, the measured increase in average radius between 200 and 150 °C cannot be reproduced. One reason may be the discrepancy between the experimental and modeled volume fraction in this temperature range. Just below 200 °C, the signal giving rise to the measured volume fraction is not captured by the model, so that it is not surprising that the experimental and modeled radiuses do not match.

### 3.2.3. Comparison of the measured and simulated particle size distribution (PSD) at the end of the cooling

To allow for a more accurate comparison of the modeled and measured radii, the simulated PSD is compared with the PSD obtained from the scattering signal. The scattering signal at the end of the cooling was fitted in the $q$ - range from 0.12 to 0.7 Å$^{-1}$ using a lognormal size distribution and the form factor of a sphere as shown in reference [47].
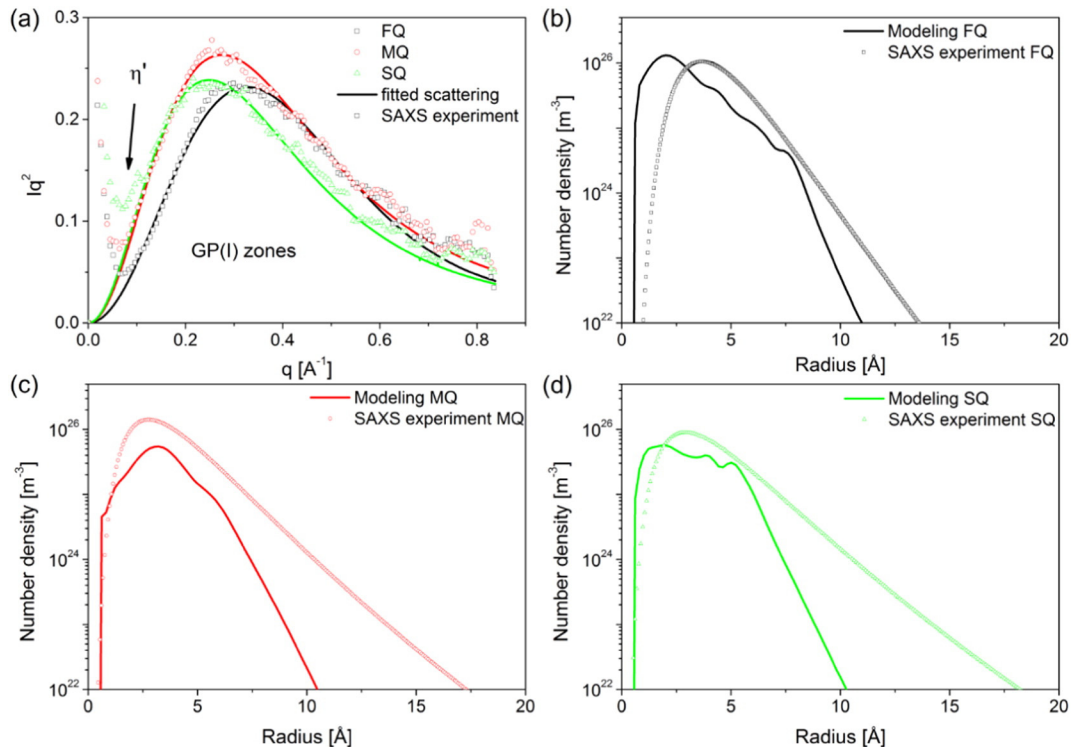


**Fig. 8.** Comparison of (a) measured and fitted scattering signal for cooling FQ, MQ and SQ at the end of the cooling and simulated and fitted PSDs after complete cooling for (b) FQ, (c) MQ and (d) SQ.

The fitted and measured scattering signals at the end of cooling are presented together in Fig. 7a. The fitted scattering curves allow reproducing relatively well the scattering contribution due to the GP(I) zones. The increasing intensity around $q = 0.07$ Å$^{-1}$ of the MQ and SQ indicates also the presence of larger (presumably η) precipitates. Fig. 8b–d show the simulated and fitted PSD for FQ, MQ and SQ at the conclusion of the cooling. Overall, the agreement between the simulations and the experiments is good at small radii for the three cases. For FQ the simulated PSD is shifted slightly to lower radii compared to the experiment results. For larger precipitate radii, differences can be observed. The PSD's obtained from SAXS extend to larger radii compared to the simulated PSD's. This could be due to homogeneous precipitates that form between 300 and 180 °C (previous section). In this temperature range the formation of precipitates cannot be modeled due to the limitations of the thermodynamic description to the GP(I) zones. However one of the limitations of the SAXS fitting arises from the fact that a pre-defined shape (lognormal size distribution) of the PSD was assumed. Overall the agreement between the simulated and measured PSD is much better compared to the measured Guinier radius and the simulated average radius. The Guinier radius is sensitive to larger radii of the PSD ($I \sim R_g^2$) and therefore overestimates the average radius of a PSD with a large dispersion. In the case of quench induced GP(I) zones it is more favorable to compare directly the PSD's.

The dispersion of the lognormal size distribution as presented in reference [25] is around 0.42 for MQ and SQ and thereby larger compared to FQ, which shows a dispersion of 0.3. This can be associated with longer time at higher temperatures, which results in larger precipitates compared to precipitates that form at lower temperatures. In general, the dispersion of the PSD is much larger than 0.2. This indicates that the Guinier radius estimated from the SAXS signal is larger than the average radius of the PSD [25].

### 3.2.4. Modeling of the dissolution of GP(I) zones after cooling FQ

The dissolution of GP(I) was modeled during continuous heating after the cooling FQ. The temperature vs. time is shown in Fig. 9a together with the calculated normalized supersaturation S of vacancies (normalized to 1 at the end of cooling). During cooling, the supersaturation of vacancies increases until room temperature. The following heating increases the vacancy mobility and leads to a rapid decrease of the supersaturation due to annihilation on defects. At 80 °C the vacancy concentration is almost at equilibrium.

Fig. 9b shows the volume fraction evolution during the entire heat treatment. The simulation matches well the experimental results during cooling, although the volume fraction evolution at near room temperature is slightly higher compared to the measured values. This was associated with a slightly overestimated diffusion at near room temperature. During the subsequent heating, the simulation shows an accelerated formation of GP(I) zones up to 116 °C. This is in contrast to the experimental results, which evidence the dissolution of the GP(I) zones between 80 and 150 °C before η′ precipitates form.

As discussed in the previous section, the broad PSD leads to an overestimated measured radius compared to the simulated average radius (Fig. 9c). During heating, the simulated radius stays constant until 116 °C. When the GP(I) zones start to dissolve, the average radius increases with increasing temperatures. The simulated increase of the average radius is similar to the measured one, except that the increase of the simulated average radius starts at higher temperatures in the simulations compared to the experiments.

Fig. 9d shows the number density of precipitates during the heat treatment. The simulated and measured (calculated) number density is seen to increase during the cooling. During heating the simulated density continues to increase up to 116 °C and then decreases because of the dissolution of the GP(I) zones. The measured density stays roughly constant up to 80 °C and then decreases until the precipitates dissolve. The differences of the absolute values of the simulated and
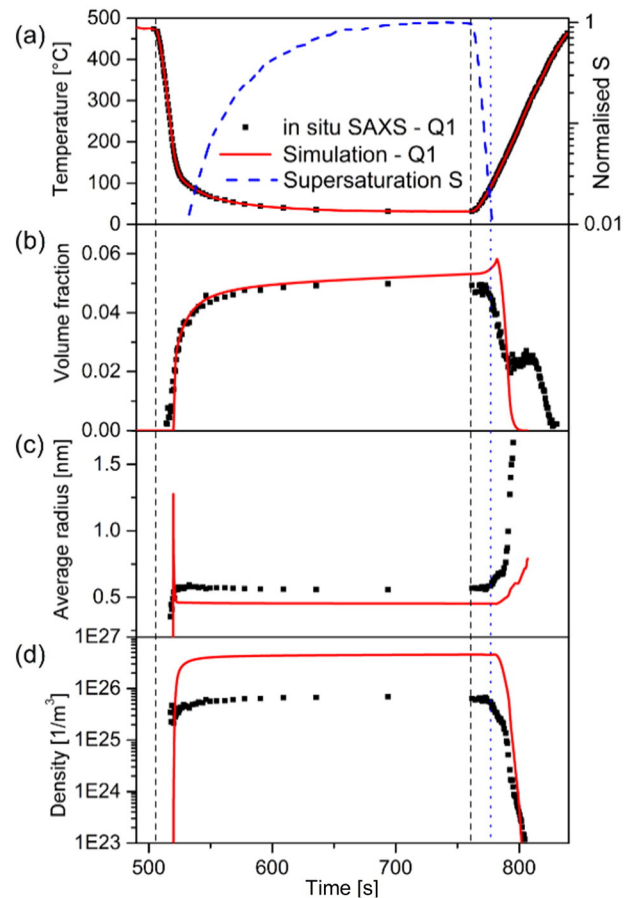


Fig. 9. Time evolution of precipitation for (a) a given temperature history corresponding to the FQ cooling followed by continuous heating showing (a) the vacancy supersaturation $S$, (b) the volume fraction, (c) the average radius and (d) the density of GP(I) zones. The dashed black lines serve as guide to the eyes for the beginning and end of the cooling.

measured density can be explained by the overestimated radius from SAXS, which leads to an underestimated density.

The differences between the simulations and the experiments during heating are explained by an overestimated effective diffusion. The high supersaturation of vacancies present after the rapid cooling decreases fast when the sample is heated up as shown in Fig. 9a. This decrease of the effective diffusion cannot be taken into account for the modeling since the effective diffusion is accounted for by adapted diffusion parameters, which are set for the cooling FQ. This is a limitation of the present modeling approach, which could be avoided when the phenomenological approach to calculate the vacancy concentration would be included in the model to account for the changes of the effective diffusion during different heat treatments. This would also avoid an under- or overestimated diffusion due to imperfect fitting as shown in Fig. 6b.

### 3.3. Quenching of an industrial 75 mm AA7449 thick plate

The calibrated precipitation model has been applied to the quench of an industrial 75 mm AA7449 thick plate. The formation of GP(I) zones is simulated for selected positions in the plate and it will be used for estimating their effect on the yield stress. The formation of heterogeneously nucleated η precipitates is not considered because (i) their amount in the plate is negligible and (ii) the solute depletion associated to these precipitates is only localized and does not affect the thermodynamic driving force away from the coarse precipitates as shown in Reference [36]. Adapted diffusion coefficients were used and obtained as explained in Section 3.3. At the surface, quarter and center positions of the plate the effective activation energies are similar with values around

**Table 3**
Fitted effective diffusion parameters for Mg at the surface, quarter and center position in the 75 mm plate.

| Cooling | $D_{0,eff}$ [m$^2$ s$^{-1}$] | $Q_{eff}$ [J mol$^{-1}$] |
|---|---|---|
| Surface | $1.40 \cdot 10^{-11}$ | 58,200 |
| Quarter | $3.99 \cdot 10^{-12}$ | 60,200 |
| Center | $4.00 \cdot 10^{-12}$ | 60,300 |

60,000 J mol$^{-1}$ as presented in Table 3. Yet, the effective diffusion coefficient at the surface position is roughly 4 times higher due to the fast cooling at high temperature, resulting in a higher vacancy supersaturation.

Fig. 10a and b show the simulated evolution of the volume fraction and the average radius during cooling at the three positions. For the different positions in the plate, different chemical compositions have been used owing to the presence of macrosegregation in thick plates [9]. For the 75 mm AA7449 thick plate, the chemical composition through-thickness profile was provided by Constellium CRV, from electron probe micro analysis (EPMA) measurements. Fig. 11 shows the normalized Zn concentration profile as function of the distance from the surface. The profile was normalized with the average Zn composition close to the surface of the plate. The Zn concentration is seen to increase slightly towards the quarter thickness of the plate. Around 25 mm from the surface, the Zn concentration decreases towards the plate center. Mg and Cu exhibit a similar segregation profile as Zn.

At the surface the GP zone formation kinetics is fast due to the supersaturation of vacancies, which leads to a 6.7% volume fraction at room temperature. The quarter position shows 6.4% volume fraction at the conclusion of the quench. This is in a similar range compared to MQ and SQ, which feature comparable cooling rates. In the center the volume fraction show the smallest value of only 3.6% at the end of the cooling.

The influence of macrosegregation is clearly evidenced by different solvus boundaries for the GP(I) zones at the different positions in the plate. The chemical composition in the surface and center position is smaller compared to the quarter position, which explains the lower solvus boundary of GP(I) zones.

The calculated evolution of the average radius is shown in Fig. 9b. The radius is highest in the surface region with 0.76 nm compared to 0.54 nm for the quarter and 0.44 nm in the center position. The fact that the highest radius and volume fraction are found at the surface where the cooling rate is highest seems counter-intuitive but is related to the high kinetics due to the high amount of excess vacancies.

Fig. 12 shows the simulated precipitation characteristics and yield strength (calculated from Eq. (5) from the modeled microstructural characteristics) at the end of the quench as function of the distance to the plate surface in the 75 mm AA7449 thick plate.

Fig. 12a presents the GP(I) zones volume fraction through the half-thickness of the plate. The highest volume fraction (7.8%) is found at 1.5 mm below the surface and the lowest at the center (4%). In general, the volume fraction is decreasing from the surface to the center, except for the surface position and at 20 mm below the surface. At the surface, a reduced solute content leads to a lower volume fraction. In contrast, at 20 mm below surface the increased solute content results in an increased volume fraction.

The average radius at the end of the quench is shown in Fig. 12b as function of the distance to the surface. The average radius shows 0.75 nm at the surface and decreases towards the center, where the average radius yields 0.44 nm. Similarly to the volume fraction, a slightly increased average radius is found at 20 mm below the plate surface.

The density of GP(I) zones is shown in Fig. 12c, which shows the opposite trend compared to the average radius. The density of GP(I) zones is lowest at the surface and increases towards the plate center. Deviations are again seen for the position at 20 mm below the surface.

The yield strength is calculated using Eq. (4) from the simulation results as presented in Fig. 12d. The highest yield strength of 288 MPa is found at 1.5 mm below the surface and the center yields the lowest yield strength of 218 MPa. The calculated yield strength in the plate at the end of the quench seems to be reasonable. Chobaut et al. reported compressive residual stresses of −300 MPa in the surface and balancing tensile residual stresses of 200 MPa in the center [19]. Therefore, the simulated yield strength in the surface of 277 MPa seems to be a good estimate when keeping in mind that plastic deformation and strain hardening occurs in the surface region. Further, the calculated yield strength of 277 MPa at the surface also compares well with the value of 275 MPa measured in the Gleeble machine [37,38]. In the center, the residual stress level yields 200 MPa and plastic deformation is not reported. Therefore, the calculated yield strength of 218 MPa seems reasonable. Unfortunately, there are no direct measurements of the precipitation characteristics in the plate right after quench, because it would be very difficult to prepare a thin foil out of a 75 mm thick plate in a sufficiently short time. However, SAXS measurements were made after several months of natural aging following the quench. They showed a volume fraction of around 10%, more homogeneous across the thickness because natural aging time homogenizes the GP(I) zone microstructure. These results are compatible with the present estimates.

## 4. Conclusion

The present work presents an approach to simulate the formation of GP(I) zones during the quenching of large industrial components. This
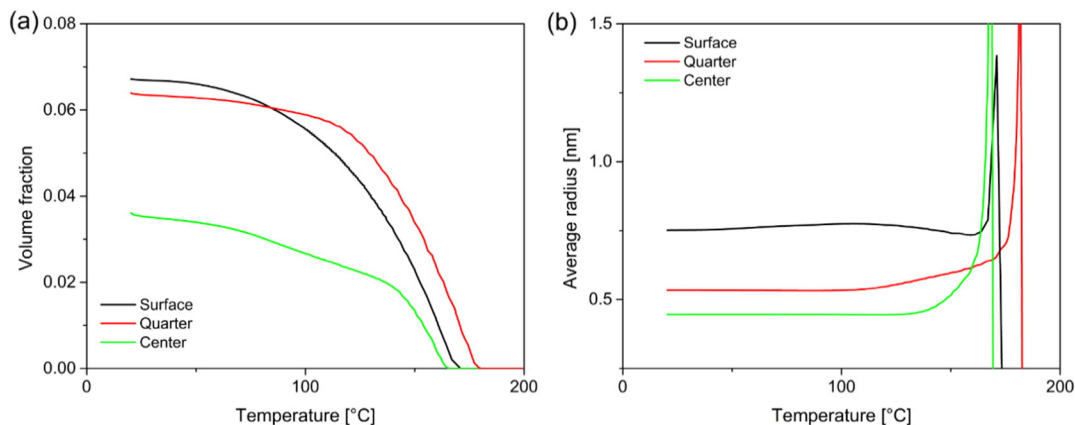


**Fig. 10.** Evolution upon cooling of (a) the volume fraction and (b) the average radius of GP(I) zones as function of temperature for the surface, quarter and center position of a 75 mm thick plate of AA7449.
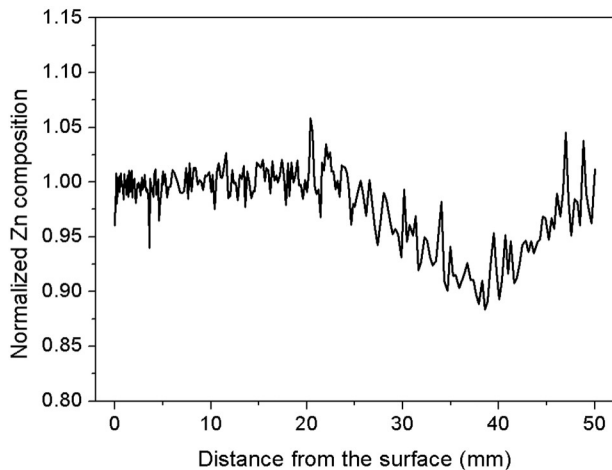
**Fig. 11.** Zn concentration as function of distance from the plate surface. The Zn concentration is normalized with the average Zn composition close to the surface of the plate.

approach consists on a continuous acquisition of GP zone precipitate characteristics during quenching and subsequent reversion, from which a precipitation class model is adjusted, including the effect of vacancy supersaturation on the diffusion coefficients. The simulation of the GP(I) zone formation is well reproduced for intermediate quench rates and in the temperature range where the residual stresses form. In particular, the effect of vacancy supersaturation is able to explain the apparently surprising lack of dependency (or even inverse effect) of quench rate on precipitated volume fraction as a function of quench rate. From the experimental data, the simulated as-quenched yield strength distribution through the thickness of AA7449 thick plates compares well against experimental results.

Still, there are several limitations of the modeling approach that need to be addressed in the future. First, applying this simple thermodynamic approach and a precipitation class model to such small objects as GP zones is questionable, and can be viewed as a way to rationalize the experimental data, more than a true physical description of the complex mechanisms of solute clustering. The present modeling approach yet provides with a practical methodology that permits fast and systematic simulations for application at processing scale when cooling rate and composition vary along the product as demonstrated in Fig. 12. Furthermore, the simplified approach is not suitable for cooling conditions that lead to substantial formation of $\eta$ at high temperatures and mechanisms for the transformation of GP zones and intermediate phases into stable phases are still not well understood. An explicit formalism of the generation and annihilation of excess vacancies should also be included in the model in order $i$ - to avoid fitting problems and $ii$ - to simulate more complex heat treatments where excess vacancies annihilate.

The coupling of the precipitation model with finite element residual stress calculations is required to predict as-quenched residual stresses in industrial Al-Zn-Mg-Cu thick plates.
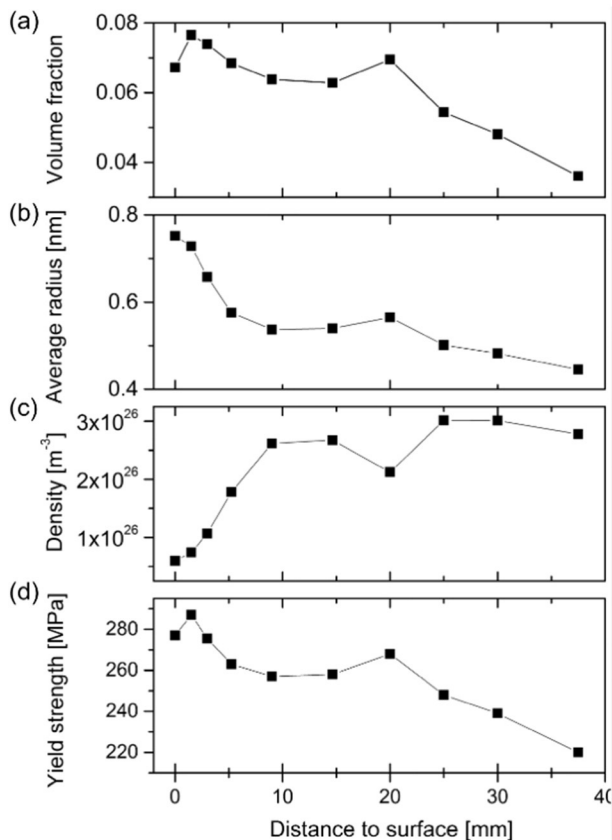
## Acknowledgements

**Fig. 12.** Simulated profile along the half-thickness of a 75 mm AA7449 plate of (a) the volume fraction, (b) the average radius and (c) the density of GP(I) zones at the end of the quench. The resulting yield strength through plate computed by the model is given in (d).

## References

[1] D. Godard, P. Archambault, E. Aeby-Gautier, G. Lapasset, Acta Mater. 50 (2002) 2319.
[2] L.K. Berg, J. Gjønnes, V. Hansen, X.Z. Li, M. Knutson-Wedel, G. Waterloo, L.R. Wallenberg, GP-zones in Al–Zn–Mg alloys and their role in artificial aging, Acta Mater. 49 (17) (2001) 3443–3451.
[3] Y.Y. Li, L. Kovarik, P.J. Phillips, Y.F. Hsu, W.H. Wang, M.J. Mills, High-resolution characterization of the precipitation behavior of an Al–Zn–Mg–Cu alloy, Philos. Mag. Lett. 92 (4) (2012) 166–178.
[4] J.Z. Liu, J.H. Chen, D.W. Yuan, C.L. Wu, J. Zhu, Z.Y. Cheng, Fine precipitation scenarios of AlZnMg (Cu) alloys revealed by advanced atomic-resolution electron microscopy study part I: structure determination of the precipitates in AlZnMg (Cu) alloys, Mater. Charact. 99 (2015) 277–286.
[5] J. Robinson, D. Tanner, C. Truman, Strain 50 (2014) 185.
[6] M.B. Prime, M.R. Hill, Scr. Mater. 46 (2002) 77.
[7] P. Lequeu, P. Lassince, T. Warner, G. Raynaud, Aircr. Eng. Aerosp. Technol. 73 (2001) 147.
[8] F. Heymes, B. Commet, B.D. Bost, P. Lassince, P. Lequeu, G.-M. Raynaud, ASM International (USA) 249 (1997).
[9] D. Godard, Influence de la Précipitation sur le Comportement Thermomécanique lors de la Trempe d'un Alliage Al-Zn-Mg-Cu(Ph.D. thesis) Institut National Polytechnique de Lorraine, (Nancy, France), 1999.
[10] Deschamps, F. Livet, Y. Brechet, Acta Mater. 47 (1998) 281.
[11] M. Dumont, W. Lefebvre, B. Doisneau-Cottignies, A. Deschamps, Acta Mater. 53 (2005) 2881.
[12] T. Morgeneyer, M. Starink, S. Wang, I. Sinclair, Acta Mater. 56 (2008) 2872.
[13] M. Reich, O. Kessler, Mater. Sci. Technol. 28 (2012) 769.
[14] Y. Xie, T. Zhou, P. Liu, C. Ma, Proceedings of the 12th International Conference on Aluminium Alloys, 2010.
[15] Y. Zhang, B. Milkereit, O. Kessler, C. Schick, P. Rometsch, J. Alloys Compd. 584 (2014) 581.
[16] Y. Zhang, M. Weyland, B. Milkereit, M. Reich, P. Rometsch, Sci. Rep. 6 (2016).
[17] P. Schloth, J.N. Wagner, J.L. Fife, A. Menzel, J.-M. Drezet, H. Van Swygenhoven, Appl. Phys. Lett. 105 (2014) 101908.
[18] M.J. Starink, B. Milkereit, Y. Zhang, P. Rometsch, Mater. Des. 88 (2015) 958.

[19] N. Chobaut, J. Repper, T. Pirling, D. Carron, J.-M. Drezet, in: H. Weiland, A.D. Rollett, W.A. Cassada (Eds.),Proceedings of the 13th International Conference on Aluminum Alloys (ICAA13), EPFL-CONF-186767 2012, pp. 285–291.
[20] R. Ferragut, A. Somoza, I. Torriani, Mater. Sci. Eng. A 334 (2002) 1.
[21] P. Kenesei, G. Horváth, S. Bernstorff, T. Ungár, J. Lendvai, Early stages of nucleation and growth of Guinier–Preston zones in Al–Zn–Mg and Al–Zn–Mg–Cu alloys, Z. Met. 97 (3) (2006) 315–320.
[22] A. Dupasquier, R. Ferragut, M.M. Iglesias, M. Massazza, G. Riontino, P. Mengucci, G. Barucca, C.E. Macchi, A. Somoza, Philos. Mag. 87 (22) (2007) 3297–3323.
[23] M. Nicolas, A. Deschamps, Acta Mater. 51 (2003) 6077.
[24] F. Zhang, J. Ilavsky, G.G. Long, J.P.G. Quintana, A.J. Allen, P.R. Jemian, Metall. Mater. Trans. A 41 (2010) 1151.
[25] A. Deschamps, F. De Geuser, J. Appl. Crystallogr. 44 (2011) 343.
[26] A. Deschamps, F. Geuser, Metall. Mater. Trans. A 44 (2012) 77.
[27] https://kur.web.psi.ch/sans1/sanssoft/sasfit.html.
[28] C.-A. Gandin, A. Jacot, Acta Mater. 55 (2007) 2539.
[29] G. Sha, A. Cerezo, Acta Mater. 52 (2004) 4503.
[30] P.V. Liddicoat, X.-Z. Liao, Y. Zhao, Y. Zhu, M.Y. Murashkin, E.J. Lavernia, R.Z. Valiev, S.P. Ringer, Nat. Commun. 1 (2010) 63.
[31] T. Marlaud, A. Deschamps, F. Bley, W. Lefebvre, B. Baroux, Acta Mater. 58 (2010) 248.
[32] M. Nicolas, Evolution de l'état de Précipitation dans un Alliage Al-Zn-Mg lors de Traitements Thermiques Anisothermes et dans la Zone Affectée Thermiquement de Joints Soudés(Ph.D. thesis) INP Grenoble, 2002.
[33] H.-G. Fabian, R. Wolter, Cryst. Res. Technol. 26 (1991) 93.
[34] C. Wolverton, Solute–vacancy binding in aluminum, Acta Mater. 55 (17) (2007) 5867–5872.
[35] G. Fribourg, Couplages Entre Précipitation et Plasticité dans un Alliage d'aluminium 7xxx: Application á des Traitements Thermomécaniques de Réduction des Distorsions(Ph.D. thesis) L'Institut Polytechnique de Grenoble, 2009.
[36] P. Schloth, Precipitation in the High Strength AA7449 Aluminium Alloy: Implications on Internal Stresses on Different Length Scales(Ph.D. thesis) EPFL, 2015.
[37] N. Chobaut, Measurements and Modelling of Residual Stress during Quenching of Thick Heat Treatable Aluminium Components in Relation to their Precipitation State(Ph.D. thesis) EPFL, 2015.
[38] N. Chobaut, D. Carron, S. Aresene, P. Schloth, J.-M. Drezet, J. Mater. Process. Technol. 222 (2015) 373–380.
[39] F. De Geuser, F. Bley, A. Deschamps, J. Appl. Crystallogr. 45 (6) (2012) 1208.
[40] Q. Puydt, S. Flouriot, S. Ringeval, F. De Geuser, R. Estevez, G. Parry, A. Deschamps, Metall. Mater. Trans. A 45 (2014) 6129.
[41] H. Löffler, I. Kovacs, J. Lendvai, J. Mater. Sci. 18 (1983) 2215.
[42] C. Mondal, A. Mukhopadhyay, Mater. Sci. Eng. A 391 (2005) 367.
[43] J. Yan, Yield Strength Modelling of Al-Cu-Mg Type Alloys(Ph.D. thesis) University of Southampton, 2006.
[44] N. Peterson, S. Rothman, Phys. Rev. B 1 (1970) 3264.
[45] S. Hirosawa, T. Sato, J. Yokota, A. Kamio, Mater. Trans. JIM 39 (1998) 139.
[46] J. Robson, P. Prangnell, Acta Mater. 49 (2001) 599.
[47] Deschamps, G. Texier, S. Ringeval, L. Delfaut-Durut, Mater. Sci. Eng. A 501 (2009) 133.